Tertiary and quaternary structure remodeling by occupancy of the substrate binding pocket in a large glutamate dehydrogenase

Melisa Lázaro [1,#], Nicolás Chamorro [2,#], Jorge P. López-Alonso [3,4], Diego Charro [1], Rodolfo M. Rasia [2,5], Gonzalo Jiménez-Osés [1,6], Mikel Valle [1,*], María-Natalia Lisa [2,5,*]

[1] Center for Cooperative Research in Biosciences (CIC bioGUNE), Basque Research and Technology Alliance (BRTA), Bizkaia Technology Park, Building 801A, 48160 Derio, Spain.

[2] Instituto de Biología Molecular y Celular de Rosario (IBR CONICET-UNR), Ocampo y Esmeralda, Rosario S2002LRK, Argentina.

[3] Instituto Biofisika (UPV/EHU, CSIC), 48940 Leioa, Spain.

[4] Basque Resource for Electron Microscopy, 48940 Leioa, Spain.

[5] Plataforma de Biología Estructural y Metabolómica (PLABEM), Ocampo y Esmeralda, Rosario S2002LRK, Argentina.

[6] Ikerbasque, Basque Foundation for Science, 48013 Bilbao, Spain.

# Equal contribution

* Correspondence: MNL: lisa@ibr-conicet.gov.ar (+54 341 423 7070; MV: mvalle@cicbiogune.es (+34 946 572 503)

Running title: Ligand-driven remodeling of mL-GDH_{180}

Total number of manuscript pages, 42; supplementary material pages, 16; tables, 1; figures, 5

Description of supplementary material including filenames:

Supplementary material.doc: Supplementary figures and tables.

Movie S1.mp4: Changes in the quaternary structure of mL-GDH_{180} detected by cryo-EM in the presence of L-glutamate and NAD^+.

Movie S2.mp4: Changes in the active site of mL-GDH_{180} detected by cryo-EM in the presence of L-glutamate and NAD^+.

Movie S3.mp4: In the presence of L-glutamate and NAD^+, a contact is established between the catalytic domains of neighboring mL-GDH_{180} subunits connected through their N-terminal regions.

ABSTRACT

Glutamate dehydrogenases (GDHs) catalyze the oxidative deamination of L-glutamate to 2-oxoglutarate using $NAD(P)^+$ as a cofactor. The large type of GDHs (L-GDHs) displays a dynamic homotetrameric architecture that alternates between open and closed states. However, the catalytic mechanism and the functional relevance of the large conformational changes in L-GDHs remain poorly understood. Here, we use cryo-EM to investigate the structure and the conformational landscape of the mycobacterial L-GDH composed of 180 kDa subunits (mL-GDH_{180}) when incubated with L-glutamate and NAD^+. Classification of the heterogeneous population of tetramers reveals opening-closing motions and sorting of individual subunits resolves the occupancy of the cofactor and substrate binding pockets. Cryo-EM maps show that ligand binding to the glutamate binding pocket is accompanied by structural changes in a region approximately two nanometers away from the active site, leading to the formation of a previously undetected interaction between the catalytic domains of neighboring subunits in mL-GDH_{180} closed tetrameric states. Our findings indicate that the occupancy of the substrate binding site of mL-GDH_{180} is linked to a remodeling of both the tertiary and quaternary structure of the enzyme.

KEYWORDS

glutamate dehydrogenase, large GDH (mL-GDH_{180}), cryo-electron microscopy, conformational dynamics, quaternary structure remodeling, substrate binding pocket, *Mycobacterium* metabolism

STATEMENT FOR A BROADER AUDIENCE

This work reveals how the binding of L-glutamate and NAD^+ reshapes the architecture of a large glutamate dehydrogenase, linking active site occupancy to long-range structural remodeling. By capturing previously unseen conformational transitions with cryo-electron microscopy, we provide insights into the molecular logic of enzyme function in mycobacteria. These findings establish a framework to understand how structural plasticity supports metabolic control.

63 **INTRODUCTION**

64 Amino acid dehydrogenases have long attracted interest due to their physiological
65 functions and potential industrial applications. Among them, glutamate
66 dehydrogenases (GDHs; EC 1.4.1.2) catalyze the reaction L-glutamate + $NAD(P)^+$ +
67 H_2O <=> 2-oxoglutarate + NAD(P)H + H^+ + NH_3, at the crossroads of carbon and
68 nitrogen metabolism. These enzymes are oligomeric and are classified based on the
69 molecular weight of their subunits. Small GDHs (S-GDHs), present in prokaryotes
70 and eukaryotes, consist of 50 kDa subunits [1]. The conserved catalytic domain spans
71 nearly the full length of the polypeptide chain of S-GDHs and mediates
72 oligomerization. Biochemical and structural studies on S-GDHs have enabled
73 detailed characterization of their catalytic and regulatory mechanisms. In contrast,
74 much less is known about large GDHs (L-GDHs), which are found in prokaryotes and
75 lower eukaryotes [2]. This group includes enzymes with 115 kDa subunits ($L\text{-}GDHs_{115}$)
76 and those with 180 kDa subunits ($L\text{-}GDHs_{180}$), such as the $L\text{-}GDH_{180}$ from
77 mycobacteria ($mL\text{-}GDH_{180}$). L-GDHs feature distinctive and extended N- and C-
78 terminal regions flanking the catalytic core, which may confer regulatory or structural
79 roles [3].

80 In a previous work, we demonstrated that the $L\text{-}GDH_{180}$ from *Mycobacterium*
81 *smegmatis* ($mL\text{-}GDH_{180}$; 76% sequence identity with the $L\text{-}GDH_{180}$ from
82 *Mycobacterium tuberculosis*) assembles into a homotetramer, with a quaternary
83 structure markedly different from that of S-GDHs [3]. Such architecture is stabilized by
84 interactions involving the N-terminal region, which contains ACT- and PAS-type
85 domains typically associated with regulatory functions [4,5], as well as a C-terminal
86 domain of unknown function. Despite such advances, the conformational landscape
87 explored by L-GDHs during catalysis remained poorly unknown.

Here we report cryo-EM structures of mL-GDH_{180} at resolutions up to 3 Å, obtained in the presence of NAD^+ and L-glutamate. We reveal that ligand binding to the glutamate binding pocket is accompanied by changes in the tertiary structure in a region approximately 2 nm distant from the active site, promoting interactions between the catalytic domains of neighboring monomers and modulating the quaternary structure.

Despite extensive efforts to understand the molecular basis of GDHs activity and regulation, structural data on ternary complexes containing enzyme, cofactor, and substrate are scarce, particularly for NAD^+-dependent L-GDHs. Here, we present cryo-EM evidence for enzyme species present upon incubation with L-glutamate and NAD^+ of a key L-GDH_{180} for the virulence of a long-attacked pathogen [6], offering new insights into the conformational plasticity of L-GDHs and setting the stage for a deeper understanding of their regulation.

102 **RESULTS**

103 **Three conformers of mL-GDH$_{180}$ detected upon incubation with L-glutamate**
104 **and NAD$^+$ reveal modulations of the enzyme quaternary structure**

105 To investigate the molecular basis of mL-GDH$_{180}$ activity, we first determined its
106 kinetic parameters for the oxidative deamination of L-glutamate. Under steady state
107 conditions, the reaction displayed a k_{cat} of (15 ± 2) s^{-1}; the estimated K_M values were
108 (40 ± 10) mM for L-glutamate and (0.19 ± 0.06) mM for NAD$^+$, yielding catalytic
109 efficiencies (k_{cat}/K_M) of (0.4 ± 0.1) mM^{-1} s^{-1} and (80 ± 30) mM^{-1} s^{-1}, respectively
110 (Figure S1A), as determined in 50 mM Hepes, 50 mM NaCl, at pH 6.8, near the
111 apparent pH optimum of the reaction (Figure S1B). Single-particle cryo-EM
112 experiments were then conducted on mL-GDH$_{180}$ incubated with NAD$^+$ and L-
113 glutamate under NADH-producing conditions, during early turnover (Figure S1C; see
114 also Materials and methods). As previously reported [3], 2D class averages revealed
115 high flexibility at the distal ends of the tetramers, where the ACT*1-2 and PAS
116 domains are located (Figure S2). This flexibility resulted in vanishing density for
117 residues 1-499 in the cryo-EM maps. Subsequently, 3D-classification of mL-GDH$_{180}$
118 particles revealed three conformational states of the enzyme, named Open (32.4%),
119 Closed1 (39.6%) and Closed2 (28%) (Figure 1, Table I, Figure S3). In these
120 conformers, the ACT*3 module, the helical motif 3 (HM3), the catalytic domain and
121 the C-terminal region were defined in each monomer, achieving estimated global
122 resolutions of 3.88 Å, 3.54 Å and 3.57 Å, respectively. The conformers differ primarily
123 in the relative positions of the subunits (Figure 1A, Figure S4A and Movie S1). In the
124 Closed forms, the catalytic domains of adjacent subunits connected through their N-
125 terminal segments are found in closer proximity compared to the Open state (Figure
126 1B).

127 Comparison of the atomic models derived from the 3D cryo-EM maps provided initial
128 insights on the molecular determinants underlying the modulation of mL-GDH_{180}
129 architecture. Pairwise structural alignments of monomers from the three conformers,
130 based on all modeled α-carbons, yielded an average RMSD (root-mean-square
131 deviation) of 0.4 Å (calculated over 1075 aligned residues), indicating that the
132 observed conformational variability primarily reflects quaternary rearrangements.
133 Consistent with this, the intersubunit contact area at the AB-CD interface (Figure
134 S4B) was measured [7] as 550 $Å^2$, 750 $Å^2$ and 800 $Å^2$, and at the AD-BC interface as
135 1200 $Å^2$, 1000 $Å^2$ and 1200 $Å^2$, for the Open, Closed1 and Closed2 forms,
136 respectively. At the AB-CD interface, hydrogen bonds between residues in the ACT*3
137 domains of neighboring monomers mediate the intersubunit contacts in all three
138 conformers (Figure S4B and Table SI). Remarkably, a previously undetected
139 interfacial interaction was found in the Closed2 tetramer, involving a hydrogen bond
140 between the side chains of Ser650 (in the HM3) and Glu790 (in the catalytic domain)
141 (Figure 1B and Figure S4B). At the AD-BC interface, distinct salt bridge combinations
142 are found in the different conformers, with Asp1516:Arg1582 present in the Open
143 form, Arg1504:Glu1562 in the Closed1 and both simultaneously observed in the
144 Closed2 (Figure S4B and Table SI). Additionally, in all three conformations, extensive
145 hydrogen bonds networks link a conserved set of secondary structure elements in
146 the C-terminal domain, with alternative arrangements in each state. Most of the
147 interfacial residues observed in mL-GDH_{180} tetramers found in the presence of NAD^+
148 and L-glutamate had been previously identified as contributors to oligomer
149 stabilization [3] and are conserved across diverse L-GDHs (Figure S5), suggesting a
150 shared structural basis for quaternary modulation within this enzyme family.

151 As HM3 in one monomer and the region encompassing Glu790 in the catalytic
152 domain of an adjacent subunit move closer, other portions of the catalytic domains in
153 mL-GDH$_{180}$ monomers linked via their N-terminal segments also shift toward each
154 other (Figure 1B). Intriguingly, the density corresponding to residues 825-838 was
155 poorly defined in the maps of the Open, Closed1 and Closed2 conformers
156 distinguished in the presence of NAD$^+$ and L-glutamate. At the same time, the
157 nicotinamide moiety of the cofactor molecule placed within the active site appeared
158 highly mobile in all three species, although this mobility seemed reduced in the
159 Closed1 and Closed2 forms. No additional density was detected within the active
160 sites beyond that attributable to the cofactor.
161
162 **Three conformers of mL-GDH$_{180}$ subunits reveal modulations in tertiary**
163 **structure associated with differential active site occupancies**
164 To clarify the absence of signal for any ligand other than the cofactor in the cryo-EM
165 maps of mL-GDH$_{180}$ tetramers, we performed a hierarchical classification of all mL-
166 GDH$_{180}$ subunits, regardless of whether they belonged to the Open, Closed1 or
167 Closed2 conformers, using a mask that covered the catalytic domain (Figure S3).
168 This classification yielded three distinct forms for mL-GDH$_{180}$ monomers, termed
169 empty-monomer, cofactor-monomer and cofactor/ligand-monomer, with estimated
170 resolutions of 3.07 Å, 2.95 Å and 3.12 Å, respectively (Figure 2 and Table I). The
171 empty-monomer map shows faint density within the cofactor binding pocket, but does
172 not reveal strong binding to that site, nor any signal in the substrate binding pocket.
173 In contrast, the cofactor-monomer map clearly displays a bound cofactor molecule in
174 the catalytic cavity and the cofactor/ligand-monomer map discloses both the cofactor
175 and an additional density element within the active site (Figure 2 and Figure S6). An

176 average of all these variants resulted in a 2.63 Å resolution map of the mL-GDH$_{180}$
177 monomer (Figure S6 and Figure S7), which was used to model the polypeptide
178 segment comprising residues 463–1588 before refining the atomic coordinates for
179 each occupancy state.
180 The atomic model derived from the empty-monomer map revealed the arrangement
181 of residues that, according to previous analyses [2,3], define the dinucleotide binding
182 region (DNBR) and the glutamate binding region (GluBR) of mL-GDH$_{180}$ (Figure 2).
183 The cryo-EM maps of the cofactor- and cofactor/ligand- monomers of mL-GDH$_{180}$
184 allowed to place a NAD$^+$ molecule in extended conformation within the DNBR (Figure
185 2). According to our models, the pyrophosphate moiety is located in the crevice
186 formed between strands β1 and β5 (residues 953-958 and 1070-1073, respectively)
187 of subdomain II of the catalytic domain (SDII) and is stabilized by the dipole of the
188 helix comprising residues 964-969, which connects strands β1 and β2 (residues 976-
189 982) and is known as the dinucleotide binding helix (Figure 3). The adenine ring of
190 NAD$^+$ fits well in the density, the glycosidic bond to the nicotinamide ring adopts a
191 *syn* conformation and both riboses display C2' *endo* puckering, in agreement with
192 previous reports for S-GDHs [8].
193 Notably, the pattern of NAD$^+$-protein interactions differs between cofactor- and
194 cofactor/ligand- mL-GDH$_{180}$ monomers (Figure 2). In the cofactor-monomer, the
195 adenine ring interacts with the side chain (sc) of Tyr1079, the 2' and 3' hydroxyl
196 groups of the adenosine ribose point towards the surface of the protein and hydrogen
197 bond Asp983 (sc) and the main chain (mc) of Asp960, respectively, phosphates
198 interact with the amide nitrogen of Asp964 and Val965, the nicotinamide ribose
199 hydrogen bonds Gly1075 (mc) and Asn1115 (mc and sc), and the nicotinamide
200 amide contacts His923 (sc), Thr929 (sc) and Asp964 (sc). In contrast, in the

201 cofactor/ligand-monomer, the adenine of NAD^+ interacts with Tyr1079 (sc) as well as
202 His984 (sc), both adenosine hydroxyls hydrogen bond Asp960 (sc and mc), the
203 nicotinamide ribose interacts only with Asn1115 (mc and sc) and the nicotinamide
204 amide contacts only Thr929 (sc) and Asp964 (sc). These differences, along with
205 subtle but detectable conformational changes in segments 958-966 and 981-987 that
206 contribute to the DNBR, correlate with a shift of the cofactor toward the GluBR in the
207 cofactor/ligand-monomer. In this state, a novel density element becomes evident
208 (Movie S2), within which it is possible to position a substrate molecule (CC = 0.79)
209 such that the α-carbon of the amino acid lies 3.3 Å from the C4 atom of the
210 nicotinamide ring of the cofactor, explaining the continuous density observed
211 between them. Hence, the γ-carboxylate of the ligand forms salt bridges with Arg780
212 (sc).
213 Strikingly, segment 914-924, which lines the active site cleft, and region 886-901,
214 which borders the glutamate binding pocket, adopt distinct conformations in the
215 empty-, cofactor- and cofactor/ligand- mL-GDH_{180} monomers (Figure 2). These
216 variations are associated with alternate conformations of segment 825-838, which is
217 better defined in the maps of the monomers than in the tetrameric reconstructions.
218 Thus, residues 825-827 and 830-838 could be built for the empty- and cofactor-
219 monomers, while residues 825 and 829-838 were modeled for the cofactor/ligand-
220 monomer. In the empty-monomer, Arg835 is directed toward Asp964 and Asp960,
221 while Asp834 faces His984. When the cofactor binds within the DNBR, engaging
222 residues Asp964, Asp960 and His984, Arg835 and Asp834 shift from their positions
223 and the segment 830-838 loosens its packing against the catalytic core. When the
224 GluBR is also occupied, segment 831-837 packs against residues 889-894. The

225 amino acid string 825-838 of mL-GDH$_{180}$ is found in L-GDHs$_{180}$ but not in related low
226 molecular weight enzymes (Figure 3 and Figure S5) [9].
227
228 **GluBR occupancy is linked to the coupling of the catalytic domains of two**
229 **adjacent monomers in the Closed mL-GDH$_{180}$ conformations**
230 To elucidate structural changes in the context of mL-GDH$_{180}$ tetramers, we next
231 discriminated the monomeric conformers according to whether they originated from
232 Open, Closed1 and Closed2. This analysis revealed nine distinct species: Open-
233 empty-monomer, Closed1-empty-monomer, Closed2-empty-monomer (3.5 Å, 3.35 Å
234 and 3.48 Å resolution, respectively), Open-cofactor-monomer, Closed1-cofactor-
235 monomer, Closed2-cofactor-monomer (3.3 Å, 3.23 Å and 3.28 Å), Open-
236 cofactor/ligand-monomer, Closed1-cofactor/ligand-monomer and Closed2-
237 cofactor/ligand-monomer (3.23 Å, 3.11 Å and 3.18 Å) (Figure S3).
238 No discernable structural differences were observed among the empty- or cofactor-
239 monomers across the tetrameric states. In contrast, cryo-EM maps of the
240 cofactor/ligand-monomers displayed heterogeneity within the glutamate binding
241 pocket. In the Open-cofactor/ligand-monomer map, a continuous density extends
242 from the cofactor nicotinamide ring into the GluBR (Figure 4, see also Figure 2),
243 although it fades in the region where the γ-carboxylate of the substrate would be
244 stabilized. Conversely, the maps of the Closed1- and Closed2-cofactor/ligand
245 monomers display ligand density within the GluBR primarily near Arg780, with a
246 weaker signal in the Closed2 state.
247 As noted earlier, incubation of mL-GDH$_{180}$ with NAD$^+$ and L-glutamate induces
248 remodeling of the region 825-838 (Figure 2). Strikingly, this segment interacts with
249 residues 704-706 of the catalytic domain of a neighboring N-terminally-linked subunit,

giving rise to an additional molecular bridge in the Closed tetramers (Figure 4). This intersubunit interaction appears strengthened in the Closed2 state (Table I). Importantly, it is only observed when the monomer contributing the 825-838 region has both its cofactor and substrate binding pockets simultaneously occupied. The interaction occurs approximately 2 nm from the active site of the ligand-loaded monomer (Movie S3), linking GluBR occupancy to the physical contact between adjacent catalytic domains and suggesting a structural basis for turnover regulation.

258 **DISCUSSION**

259 GDHs constitute a large family of enzymes that function in all kingdoms of life at the
260 crossroad between the Krebs cycle and ammonium assimilation. While S-GDHs have
261 been studied for over half a century, it was not until 2021 that the first experimental
262 evidence of the 3D architecture of an L-GDH was obtained [3]. In that work, we
263 determined that the quaternary structure of mL-GDH$_{180}$ differs radically from that of
264 S-GDHs, and that such assembly is shaped by the distinctive N- and C-terminal
265 extensions characteristic of L-GDHs [3]. Here we present cryo-EM data reaching
266 resolutions up to 2.63 Å for mL-GDH$_{180}$ (Table I), captured in the presence of NAD$^+$
267 during the oxidative deamination of L-glutamate.

268 Our 3D classification of subunits successfully separated mL-GDH$_{180}$ monomers with
269 both the DNBR and GluBR simultaneously occupied, as well as monomers bound to
270 NAD$^+$ alone (Figure 1, Figure 2 and Figure 4). The NAD$^+$ binding mode in mL-GDH$_{180}$
271 (Figure 2 and Figure 4) mirrors that described for *Cs*GDH (S-GDH from *Clostridium*
272 *symbiosum*) [8]. The adenine ring is stabilized by hydrogen bonds with His984 (Pro262
273 in *Cs*GDH) and Tyr1079 (Asp325), the NH and CO groups of the nicotinamide amide
274 contact Asp964 (Asn240) and Thr929 (Thr209), respectively, the phosphates interact
275 with Asp964 and Val965 (Val241), while the nicotinamide ribose hydrogen bonds
276 Gly1075 (Ala321) and Asn1115 (Asn347). On the other hand, the 2'-OH of the
277 adenosine ribose, along with the 3'-OH, interacts with Asp960 (Phe238) and is
278 additionally surrounded by Asp983 (Gly261) and His984, occupying a relatively more
279 spacious pocket than in *Cs*GDH [8]. Considering that His984 and Arg985 (Asp263)
280 might stabilize the 2'-phosphate of NADP$^+$, one possible explanation for mL-GDH$_{180}$
281 specificity for NAD$^+$ [10,11] is that this enzyme, as well as related L-GDHs [2,12–17],
282 evolved to favor NAD$^+$ via the interactions of the 2'-OH group with Asp960 and

283 Asp983. These residues might also exert a repulsive effect on the 2'-phosphate of
284 $NADP^+$. This interpretation aligns with previous suggestions that NAD^+ specificity is
285 determined by interactions between the 2'-OH of the adenosine ribose and both the
286 Gly-rich loop (GxGxxA/S, as defined in L-$GDHs_{180}$ [2]) and an acidic residue at the so-
287 called position 7 (Asp983 in mL-GDH_{180}) of the fingerprint region of the nucleotide
288 binding fold [18,19].
289 A seminal study on *Cs*GDH established that amino acid specificity is conferred by
290 Lys89 and Ser380, which interact with the γ-carboxylate of the substrate [20]. In mL-
291 GDH_{180}, Arg780 (Lys89) is suitably positioned to form salt bridges with the γ-
292 carboxylate of L-glutamate (Figure 2). Though the hydroxyl of Ser1147 (Ser380) lies
293 4.3 Å from the γ-carboxylate of L-glutamate, slightly beyond hydrogen bond range, its
294 position corresponds to that of Ser360 in *Cs*GDH. Also, residues Ala886 and
295 Val1144 (Ala163 and Val377), Gly814 and Ala815 (Gly122 and Gly123), Gly781 and
296 Gly782 (Gly90 and Gly91) and Gly1143 (Gly376), previously highlighted for their
297 roles in establishing hydrophobic interactions with the γ- and δ-carbons of L-
298 glutamate, shaping the L-glutamate binding pocket, orienting functional groups in the
299 catalytic center and being located near the binding site of the nicotinamide ring of the
300 dinucleotide, respectively [20], are similarly arranged in the mL-GDH_{180} cofactor/ligand-
301 bound monomers. This structural similitudes underscore the conservation of key
302 amino acid specificity determinants in mL-GDH_{180} (and related L-GDHs; see Figure
303 S5 and [2]) and S-GDHs.
304 Our steady-state data support an ordered sequential mechanism for the oxidative
305 deamination of L-glutamate catalyzed by mL-GDH_{180}, in which NAD^+ binds first to the
306 active site, followed by L-glutamate; chemistry then ensues, 2-oxoglutarate is
307 released first, and NADH leaves last (Figure S1D and S1E). In line with this, our

308 cryo-EM 3D classifications recovered empty, cofactor and cofactor/ligand monomer
309 species but not a distinct ligand-only class of subunits. Moreover, given the
310 conservation of residues that mediate catalysis, L-GDHs are expected to function
311 similarly to S-GDHs [3,20]. Our atomic model of the mL-GDH_{180} cofactor/ligand-
312 monomer aimed to account for the density observed in the GluBR (Figure 2). In this
313 model, the α-carboxylate and amino groups of L-glutamate adopt a slightly different
314 orientation than in *Cs*GDH [20]. Although the α-carboxylate of L-glutamate faces
315 Lys806 (Lys113), their separation (4.1 Å) is longer than ideal for direct interaction.
316 Similarly, the α-carboxylate of the substrate lies 6.4 Å from the side chain of Gln803
317 (Gln110), and the amino group is 4.9 Å from the carbonyl of Ala887 (Gly164) and 6.7
318 Å from the side chain of the catalytic Asp888 (Asp165). It is worth noting that, at our
319 working resolution, we cannot detect water molecules that might contribute to
320 substrate stabilization within the active site. Besides, the packing of residues 825-838
321 against segment 889-894 may help stabilize the position of Asp888, even though its
322 side chain is only partially defined in cryo-EM maps. Certainly, catalysis is expected
323 to involve a localized conformational adjustment that enables the side chain of
324 Asp888 to approach the substrate's amino group for proton abstraction in the first
325 step of the reaction [20]. Nevertheless, the cofactor/ligand-monomer maps (Figure 2
326 and Figure 4) reveal density corresponding to a group modeled as the α-carbon of L-
327 glutamate, located 3.2 Å from the C4 atom of the cofactor nicotinamide, and density
328 3-3.5 Å from the Ala887 carbonyl, consistent with the position of the leaving NH_3
329 group during catalysis [20].
330 Taken together with previous findings [3], our data confirm that mL-GDH_{180} exhibits
331 pronounced conformational flexibility. In the absence of ligands, the enzyme
332 populates two tetrameric forms, Open and Closed, detected at 4.19 and 6.6 Å

333 resolution, respectively [3]. In the present study, under conditions of saturating NAD^+
334 (4 mM) and sub-saturating L-glutamate (42 mM) (see also Figure S1), three
335 tetrameric states, Open, Closed1 and Closed2, were observed, with evidence of
336 DNBR occupancy across the full ensemble (Figure 1). Thus, compared to the ligand-
337 free state, these conditions appear to shift the conformational equilibrium toward the
338 Closed forms. The segment 825-838 adopts distinct geometries depending on
339 whether the cofactor is anchored to the DNBR and whether L-glutamate (or
340 derivatives thereof) is present in the GluBR (Figure 2). In monomers where both
341 regions are simultaneously occupied (cofactor/ligand-monomers), the conformation
342 of this segment is compatible with an interaction with residues 704-706 of the N-
343 terminally linked neighboring subunit in Closed tetramers (Figure 4).
344 Unlike in S-GDH [20,21], we did not observe changes in the relative positions of SDI and
345 SDII within the catalytic domain of mL-GDH_{180}. Instead, conformational transitions
346 among oligomeric states were accompanied by adjustments at the ACT*3 and C-
347 terminal domain interfaces, changes in the intersubunit contact between residues
348 650 (in the HM3) and 790 (in the catalytic domain), and the linkage between
349 segments 825-838 and 704-706 (both in the catalytic domain), the latter forming only
350 in Closed tetramers when both substrate and cofactor occupy the active site (Figure
351 5). These long-range transitions are presumably slower than catalysis and are thus
352 observable in our experiment. While our data do not permit conclusions about
353 positional and/or compositional heterogeneity within the GluBR or DNBR during
354 catalysis, the most reasonable scenario is that the reaction occurs when both regions
355 are loaded (Figure 4), with the cofactor approaching the substrate binding pocket
356 (Figure 2). Overall, our results indicate that the 825-838/704-706 bridge acts as a
357 closure-dependent modulator that biases the co-occupied Open-Closed equilibrium

358 and tunes the dwell time of the Closed ternary complex; the net effect on turnover is
359 expected to reflect the kinetic balance between chemistry and product release under
360 the conditions considered.
361 Notably, in the absence of added effectors, we found no evidence of cooperativity for
362 mL-GDH$_{180}$ catalyzed L-glutamate oxidation across pH 6.0–7.1, an interval that
363 spans the reaction's apparent pH optimum (Figure S1B) and overlaps the
364 physiological pH range [22,23]. At pH 6.8, the initial-rate dependences on L-glutamate
365 and on NAD^+ were Michaelis–Menten both when the co-substrate was fixed at a
366 saturating concentration and when it was held at several subsaturating levels (Figure
367 S1D). Consistent with this trend, datasets acquired at pH 6.5 (the condition used for
368 cryo-EM specimen preparation) were likewise well described by Michaelis–Menten
369 kinetics. Thus, within this near-optimal pH window, steady-state behavior is
370 consistent with independent active sites. The structural origin of departures from this
371 pattern at basic pH (this work and [10]) and under activity modulators [3,10] remains to be
372 determined, particularly given the regulatory potential of the N- and C-terminal
373 regions of the enzyme.
374 We found that ligand binding to the active (orthosteric) site of mL-GDH$_{180}$ is linked to
375 tertiary structure changes that lead to the consolidation of an oligomeric interface two
376 nanometers away from the catalytic center [24]. It is worth considering whether and
377 how natural or designed molecules binding to the 825-838 and/or 704-706 segments
378 could influence catalysis and whether occupancy of the active site modulates such
379 regulation [25]. Our findings open new avenues for high-resolution studies on catalysis
380 and regulation of L-GDHs of medical and industrial relevance.
381

382 **MATERIALS AND METHODS**

383 **Protein production**

384 Plasmid pLIC-His-mL-GDH_{180} [3] was used to produce N-terminally His6-tagged mL-
385 GDH180 (MSMEG_4699, Uniprot A0R1C2) in *E. coli* cells. Transformed *E. coli*
386 BL21(DE3) cells were grown at 37 °C in LB broth supplemented with 100 µg/ml
387 ampicillin until reaching 0.8 units of optical density at 600 nm. Protein expression was
388 then induced by adding isopropyl β-D-1-thiogalactopyranoside (IPTG) to a final
389 concentration of 0.5 mM and incubation was continued for 18 hours at 14 °C. The
390 culture was centrifuged and the pellet was resuspended in 25 mM Hepes, 500 mM
391 NaCl, 10 % V/V glycerol, 10 mM imidazole, pH 8.0. The suspension was
392 supplemented with 0.01 µg/ml DNAse, 4 µM $MgSO_4$ and the protease inhibitor
393 cOmplete™ EDTA-free Protease Inhibitor Cocktail (Roche). Cells were then
394 sonicated and the mixture was clarified by centrifugation. The supernatant was
395 loaded onto a HisTrap HP column (Cytiva) equilibrated with buffer 25 mM Hepes,
396 500 mM NaCl, 10% v/v glycerol, 20 mM imidazole, pH 8.0, and His6-tagged mL-
397 GDH_{180} was purified by applying a linear imidazole gradient (20-500 mM). The
398 protein was then further purified by size-exclusion chromatography, using a
399 Superose 6 10/300 GL column (Cytiva) equilibrated in 20 mM Mes, 300 mM NaCl,
400 pH 6.5. mL-GDH_{180} containing fractions, as confirmed by SDS-PAGE, were pooled
401 and used immediately or stored at -80 °C for use in subsequent studies. The protein
402 was quantified by electronic absorption using the molar absorption coefficient of
403 171,090 M^{-1} cm^{-1}, predicted from the amino acid sequence by the ProtParam tool
404 (http://web.expasy.org/protparam/).

405

406 **Steady state kinetics**

407 Reactions were performed at 25 °C, using 10 nM mL-GDH_{180}. Oxidative deamination
408 of L-glutamate catalyzed by mL-GDH_{180} was monitored by the increase in
409 absorbance at 340 nm due to NADH production (ε_{340} = 6220 M^{-1} cm^{-1}) on a
410 Shimadzu UV-120-02 spectrophotometer. Initial rate measurements were carried out
411 in the following buffers: 50 mM Mes, 50 mM NaCl, pH 6.0; 50 mM Mes, 50 mM NaCl,
412 pH 6.5; 50 mM Hepes, 50 mM NaCl, pH 6.8; 50 mM Hepes, 50 mM NaCl, pH 7.5; 50
413 mM Hepes, 50 mM NaCl, pH 8.2; 30 mM sodium phosphate buffer, pH 7.1; 30 mM
414 sodium phosphate buffer, pH 8.0. Within pH 6.0–7.1, the kinetic parameters k_{cat} and
415 K_M were obtained by fitting the dependence of the initial rate on substrate
416 concentration to the Michaelis-Menten equation (Figure S1). At pH 7.5, the
417 dependence of the initial rate on substrate concentration was sigmoidal; accordingly,
418 data were fitted to the Hill equation. Parameter estimation for Michaelis-Menten and
419 Hill models was performed by nonlinear regression. At pH 8.0 and 8.2, where activity
420 was low and the rate-substrate relationship remained essentially linear across the full
421 substrate range, catalytic efficiency (k_{cat}/K_M) was obtained by linear regression of rate
422 versus substrate concentration. Each experiment was performed at least twice, in
423 some cases using independent protein preparations. When error bars are shown on
424 kinetic parameters, they represent the standard errors from curve fitting. Mean k_{cat}
425 and K_M values reported in the text include errors obtained by propagating the
426 standard errors from individual fits across replicates; catalytic efficiency was
427 calculated as k_{cat}/K_M with error propagated from those parameter errors.
428
429 **Cryo-electron microscopy**
430 4 µl of a mixture containing 42 mM L-glutamate, 4 mM NAD^+ and 0.125 mg/ml mL-
431 GDH_{180} was prepared in 20 mM Mes, 300 mM NaCl, pH 6.5, at 10 ºC, using a buffer

432 closely aligned with conditions previously optimized for single-particle analysis [3].
433 Samples were applied to Quantifoil R2/2 holey carbon grids and vitrified using a
434 Leica EM GP2 within the first minute after mixing, during which enzymatic activity
435 was confirmed by an increase in absorbance at 340 nm (Figure S1C), indicative of
436 NADH production. In addition, a similar protein solution was applied onto the same
437 type of grids bearing an additional thin layer of carbon. Vitrification on these two
438 types of grids was required to obtain top and side views of mL-GDH_{180} tetramers
439 (Figure S2). Data collection was carried out in a ThermoFisher Titan Krios G4
440 transmission electron microscope paired with a Gatan BioContinuum Imaging Filter
441 and a K3 direct electron detector, at the BREM (Basque Resource for Electron
442 Microscopy). 23,747 and 19,038 movie frames were acquired for the sample on R2/2
443 grids and grids supplemented with an additional thin layer of carbon, respectively
444 (Figure S2). Both collections were performed at a nominal magnification of ×130,000,
445 resulting in a sampling of 0.6462 Å/pixel. Each movie contained 50 frames with an
446 accumulated dose of 49 $e^-/Å^2$. Movie frames were aligned using MotionCor2 [26] and
447 the final average included all dose-weighted frames.
448 The contrast transfer function (CTF) of the micrographs was estimated using
449 CTFFIND4 [27]. Particles were automatically selected from the micrographs using
450 autopicking from RELION-4 [28]. To speed up calculations, particles were extracted
451 with a 2x binning, resulting in a pixel size of 1.29 Å/pixel. In datasets with potential for
452 high resolution, particles were re-extracted at original sampling. An initial set of
453 667,866 particles was subjected to 2D and 3D classification procedures (Figure S3).
454 The 3D-classification with imposed D2 symmetry resulted in eight different classes,
455 but only three achieved good definition and high resolution. Three different
456 conformations were obtained, called the Open (37,641 particles), Closed1 (45,998

457 particles) and Closed2 (32,441 particles) conformations, with estimated resolutions of
458 3.88 Å, 3.54 Å and 3.57 Å, respectively. Each class was symmetry-expanded, the
459 star files were joined (116,080x4, *i.e.* 464,320 particles) and an average 3D map of a
460 subunit was refined using a mask and polished to a final resolution of 2.63 Å. A 3D
461 classification within a sphere mask focused on the active site separated three
462 different states: empty-monomer, with 131,216 particles and 3.07 Å of resolution,
463 cofactor-monomer, with 168,668 particles and 2.95 Å of resolution, and
464 cofactor/ligand-monomer, with 112,701 particles and 3.12 Å of resolution. These
465 three groups were crossed (common particles between selection files) with the three
466 sets of particles obtained in the initial classification from the conformational changes
467 of the tetramer, resulting in nine groups of particles that were refined independently
468 (Figure S3). The three maps with signal in the cofactor and substrate binding pockets
469 were subjected to polishing and ctfrefine to improve the resolution, each one coming
470 from a conformation of the tetramer: Open-cofactor/ligand-monomer (3.23 Å),
471 Closed1-cofactor/ligand-monomer (3.11 Å) and Closed2-cofactor/ligand-monomer
472 (3.18 Å). The resolution of the cryo-EM density maps was estimated using a
473 threshold of 0.5 in the Fourier Shell Correlation (FSC) between independently
474 processed halfmaps, *i.e.*, gold standard. The cryo-EM density maps were
475 postprocessed by local sharpening using EMReady [29], which improved the structural
476 details and facilitated the atomic model building.
477 Model fitting into cryo-EM maps was performed using the programs UCSF Chimera
478 [30], Coot [31] and phenix.real_space_refine [32]. From the 2.63 Å resolution cryo-EM map
479 of a mL-GDH$_{180}$ monomer and the atomic coordinates from the Protein Data Bank
480 entry 7A1D, a model of the polypeptide chain was refined which was then fitted into
481 the other cryo-EM maps. After removing parts of the model not defined in the maps,

482 performing manual model building when necessary and placing ligands manually,
483 using Coot [31], where appropriate, atomic coordinates and B-factors were refined
484 using phenix.real_space_refine [32] with NCS and secondary structure restraints.
485 RMSDs between models were calculated using Coot [31]. Figures were generated and
486 rendered with UCSF Chimera [30] or PyMOL version 1.8.x (Schrödinger, LLC).

487 Cryo-EM maps obtained for mL-GDH_{180} were deposited in the Electron Microscopy
488 Data Bank under the accession codes EMD-52419 (Open), EMD-52420 (Closed1),
489 EMD-52421 (Closed2), EMD-52422 (empty-monomer), EMD-52423 (cofactor-
490 monomer), EMD-52424 (cofactor/ligand-monomer), EMD-52425 (Open-
491 cofactor/ligand-monomer), EMD-52426 (Closed1-cofactor/ligand-monomer), EMD-
492 52427 (Closed2-cofactor/ligand-monomer), EMD-52428 (total-monomer) and EMD-
493 52429 (Closed2-cofactor/ligand-tetramer). Atomic coordinates were deposited in the
494 Protein Data Bank under the accession codes 9HUX (Open), 9HUY (Closed1), 9HUZ
495 (Closed2), 9HV0 (empty-monomer), 9HV4 (cofactor-monomer), 9HV5
496 (cofactor/ligand-monomer) and 9HV6 (total-monomer).

497

498 **SUPPLEMENTARY MATERIAL**

499 Supplementary material.doc: Supplementary figures and tables.

500 Movie S1.mp4: Changes in the quaternary structure of mL-GDH_{180} detected by cryo-
501 EM in the presence of L-glutamate and NAD^+.

502 Movie S2.mp4: Changes in the active site of mL-GDH_{180} detected by cryo-EM in the
503 presence of L-glutamate and NAD^+.

504 Movie S3.mp4: In the presence of L-glutamate and NAD^+, a contact is established
505 between the catalytic domains of neighboring mL-GDH_{180} subunits connected
506 through their N-terminal regions.

507

508 **ACKNOWLEDGMENTS**

509 This work was supported by grants PICT 2019-00989 and PICT 2021-00253 from the
510 Agencia Nacional de Promoción de la Investigación, el Desarrollo Tecnológico y la
511 Innovación (Agencia I+D+i, Argentina) to MNL as well as grants PID2021-124074NB-
512 I00 and PID2021-125946OB-I00 from Agencia Estatal de Investigación of Spain to
513 MV and GJO, respectively. We also thank the Severo Ochoa Center of Excellence
514 Accreditation CEX2021-001136-S. MNL is a career investigator from Consejo
515 Nacional de Investigaciones Científicas y Técnicas (CONICET, Argentina). NC holds
516 a CONICET PhD fellowship. NC and MNL are grateful to Liliana Rojas for excellent
517 technical assistance. Some of this work was performed at the Basque Resource for
518 Electron Microscopy located at Instituto Biofisika (UPV/EHU, CSIC), supported by the
519 Department of Science, Universities and Innovation and the Innovation Fund of the
520 Basque Government, with additional support from MCIN (Recovery, Transformation
521 and Resilience Plan) and the Basque Government “Biotechnology Complementary

Plan Applied to Health" with funding from European Union NextGenerationEU (PRTR-C17.I1; PRTR-C17.I01.P01.S13) (AAAA_ACG_AY_2539/22_05).

AUTHOR CONTRIBUTIONS

ML produced protein, prepared EM samples, performed EM experiments, processed and analyzed EM data and performed structural analyses; NC produced protein, performed kinetic analyses, analyzed EM data and performed structural analyses; JPLA collected and analyzed EM data; DC assisted during processing of EM data; RMR performed structural analyses; GJO performed structural analyses; MV designed experiments, supervised EM data collection and processing and analyzed results; MNL designed experiments, supervised biochemical experiments, refined atomic models, analyzed data and wrote the paper. All authors read and corrected the paper.

COMPETING INTERESTS

The authors declare no competing interests.

539 **REFERENCES**

540 1. Li M et al. Glutamate dehydrogenase: Structure, allosteric regulation, and role in
541 insulin homeostasis. Neurochemical Research. 2014;39(3):433–445.
542 https://doi.org/10.1007/s11064-013-1173-2
543 2. Miñambres B, Olivera ER, Jensen RA, Luengo JM. A new class of glutamate
544 dehydrogenases (GDH): Biochemical and genetic characterization of the first
545 member, the AMP-requiring NAD-specific GDH of Streptomyces clavuligerus. Journal
546 of Biological Chemistry. 2000;275(50):39529–39542.
547 https://doi.org/10.1074/jbc.M005136200
548 3. Lázaro M et al. 3D architecture and structural flexibility revealed in the subfamily of
549 large glutamate dehydrogenases by a mycobacterial enzyme. Communications
550 Biology. 2021;4(1):684. http://dx.doi.org/10.1038/s42003-021-02222-x.
551 https://doi.org/10.1038/s42003-021-02222-x
552 4. Lang EJM et al. Allosteric ACTion: The varied ACT domains regulating enzymes of
553 amino-acid metabolism. Current Opinion in Structural Biology. 2014;29:102–111.
554 https://doi.org/10.1016/j.sbi.2014.10.007
555 5. Möglich A, Ayers RA, Moffat K. Structure and Signaling Mechanism of Per-ARNT-
556 Sim Domains. Structure. 2009;17(10):1282–1294.
557 https://doi.org/10.1016/j.str.2009.08.011
558 6. Gallant JL, Viljoen AJ, Van Helden PD, Wiid IJF. Glutamate dehydrogenase is
559 required by mycobacterium bovis BCG for resistance to cellular stress. PLoS ONE.
560 2016;11(1):1–14. https://doi.org/10.1371/journal.pone.0147706
561 7. Krissinel E, Henrick K. Protein interfaces, surfaces and assemblies' service PISA
562 at the european bioinformatics institute. Journal of Molecular Biology.
563 2007;372(3):774–797. http://www.ebi.ac.uk/pdbe/prot_int/pistart.html

564 8. Baker PJ et al. Subunit assembly and active site location in the structure of
565 glutamate dehydrogenase. Proteins: Structure, Function, and Bioinformatics.
566 1992;12(1):75–86. https://doi.org/10.1002/prot.340120109
567 9. Britton KL, Baker PJ, Rice DW, Stilllman TJ. Structural relationship between the
568 hexameric and tetrameric family of glutamate dehydrogenases. European Journal of
569 Biochemistry. 1992;209(3):851–859. https://doi.org/10.1111/j.1432-
570 1033.1992.tb17357.x
571 10. O'Hare HM et al. Regulation of glutamate metabolism by protein kinases in
572 mycobacteria. Molecular Microbiology. 2008;70(6):1408–1423.
573 https://doi.org/10.1111/j.1365-2958.2008.06489.x
574 11. Nott TJ et al. An intramolecular switch regulates phosphoindependent FHA
575 domain interactions in Mycobacterium tuberculosis. Science Signaling.
576 2009;2(63):ra12. https://doi.org/10.1126/scisignal.2000212
577 12. Veronese FM et al. Nicotinamide adenine dinucleotide specific glutamate
578 dehydrogenase of Neurospora. I. Purification and molecular properties. Journal of
579 Biological Chemistry. 1974;249(24):7922–7928. https://doi.org/10.1016/S0021-
580 9258(19)42053-X
581 13. Lu CD, Abdelal AT. The gdhB gene of Pseudomonas aeruginosa encodes an
582 arginine-inducible NAD+-dependent glutamate dehydrogenase which is subject to
583 allosteric regulation. Journal of Bacteriology. 2001;183(2):490–499.
584 https://doi.org/10.1128/JB.183.2.490-499.2001
585 14. Camardella L et al. The Antarctic Psychrobacter sp. TAD1 has two cold-active
586 glutamate dehydrogenases with different cofactor specificities. Characterisation of
587 the NAD+-dependent enzyme. Comparative Biochemistry and Physiology - A
588 Molecular and Integrative Physiology. 2002;131(3):559–567.

https://doi.org/10.1016/S1095-6433(01)00507-4

15. Kawakami R, Sakuraba H, Ohshima T. Gene cloning and characterization of the very large NAD-dependent L-glutamate dehydrogenase from the psychrophile Janthinobacterium lividum, isolated from cold soil. Journal of Bacteriology. 2007;189(15):5626–5633. https://doi.org/10.1128/JB.00496-07

16. Kawakami R, Oyama M, Sakubara H, Ohshima T. The Unique Kinetic Behavior of the Very Large NAD-Dependent Glutamate Dehydrogenase from Janthinobacterium lividum. Bioscience, Biotechnology, and Biochemistry. 2010;74(4):884–887. http://www.tandfonline.com/doi/full/10.1271/bbb.90925. https://doi.org/10.1271/bbb.90925

17. Beaufay F et al. A NAD-dependent glutamate dehydrogenase coordinates metabolism with cell division in Caulobacter crescentus. The EMBO Journal. 2015;34(13):1786–1800. http://emboj.embopress.org/cgi/doi/10.15252/embj.201490730. https://doi.org/10.15252/embj.201490730

18. Baker PJ et al. Structural consequences of sequence patterns in the fingerprint region of the nucleotide binding fold. Implications for nucleotide specificity. Journal of Molecular Biology. 1992;228(2):662–671. https://doi.org/10.1016/0022-2836(92)90848-E

19. Engel PC. Glutamate dehydrogenases: The why and how of coenzyme specificity. Neurochemical Research. 2014;39(3):426–432. https://doi.org/10.1007/s11064-013-1089-x

20. Stillman TJ, Baker PJ, Britton KL, Rice DW. Conformational flexibility in glutamate dehydrogenase: Role of water in substrate recognition and catalysis. Journal of Molecular Biology. 1993;234(4):1131–1139.

https://doi.org/10.1006/jmbi.1993.1665

21. Borgnia MJ et al. Using cryo-EM to map small ligands on dynamic metabolic enzymes: Studies with glutamate dehydrogenase. Molecular Pharmacology. 2016;89(6):645–651. https://doi.org/10.1124/mol.116.103382

22. Rao M, Streur TL, Aldwell FE, Cook GM. Intracellular pH regulation by Mycobacterium smegmatis and Mycobacterium bovis BCG. Microbiology. 2001;147(4):1017–1024. https://doi.org/10.1099/00221287-147-4-1017

23. Vandal OH et al. A membrane protein preserves intrabacterial pH in intraphagosomal Mycobacterium tuberculosis. Nature Medicine. 2008;14(8):849–854. https://doi.org/10.1038/nm.1795

24. Perica T, Chothia C, Teichmann SA. Evolution of oligomeric state through geometric coupling of protein interfaces. Proceedings of the National Academy of Sciences. 2012;109(21):8127–8132. http://www.pnas.org/cgi/doi/10.1073/pnas.1120028109. https://doi.org/10.1073/pnas.1120028109

25. Schulze JO et al. Bidirectional Allosteric Communication between the ATP-Binding Site and the Regulatory PIF Pocket in PDK1 Protein Kinase. Cell Chemical Biology. 2016;23(10):1193–1205. http://europepmc.org/abstract/med/27693059. https://doi.org/10.1016/j.chembiol.2016.06.017

26. Zheng SQ et al. MotionCor2: anisotropic correction of beam-induced motion for improved cryo-electron microscopy. Nature Methods. 2017;14(4):331–332. https://doi.org/10.1038/nmeth.4193. https://doi.org/10.1038/nmeth.4193

27. Rohou A, Grigorieff N. CTFFIND4: Fast and accurate defocus estimation from electron micrographs. Journal of Structural Biology. 2015;192(2):216–221. https://doi.org/10.1016/j.jsb.2015.08.008

28. Zivanov J et al. New tools for automated high-resolution cryo-EM structure determination in RELION-3 Egelman EH, Kuriyan J, editors. eLife. 2018;7:e42166. https://doi.org/10.7554/eLife.42166. https://doi.org/10.7554/eLife.42166

29. He J, Li T, Huang SY. Improvement of cryo-EM maps by simultaneous local and non-local deep learning. Nature Communications. 2023;14(1):1–16. https://doi.org/10.1038/s41467-023-39031-1

30. Pettersen EF et al. UCSF Chimera - A visualization system for exploratory research and analysis. Journal of Computational Chemistry. 2004;25(13):1605–1612. https://doi.org/10.1002/jcc.20084

31. Emsley P, Lohkamp B, Scott WG, Cowtan K. Features and development of Coot. Acta Crystallographica Section D: Biological Crystallography. 2010;66(4):486–501. https://doi.org/10.1107/S0907444910007493

32. Afonine P V. et al. Real-space refinement in PHENIX for cryo-EM and crystallography. Acta Crystallographica Section D: Structural Biology. 2018;74(6):531–544. https://doi.org/10.1107/S2059798318006551. https://doi.org/10.1107/S2059798318006551

33. Abramson J et al. Accurate structure prediction of biomolecular interactions with AlphaFold 3. Nature. 2024;630(8016):493–500. http://dx.doi.org/10.1038/s41586-024-07487-w. https://doi.org/10.1038/s41586-024-07487-w

659 **TABLES**

660 **Table I. Cryo-EM data collection and processing.** LS, local sharpening.

661

	Open (EMD-52419)	Closed1 (EMD-52420)	Closed2 (EMD-52421)
Data collection and			
Magnification	130,000	130,000	130,000
Voltage (kV)	300	300	300
Electron dose ($e^-/Å^2$)	0.979	0.979	0.979
Defocus range (μm)	1.0-1.6	1.0-1.6	1.0-1.6
Pixel size (Å)	1.29	1.29	1.29
Symmetry imposed	D2	D2	D2
Initial particles images (no.)	667,866	667,866	667,866
Final particles images (no.)	37,641	45,998	32,441
Map resolution (Å)	3.88	3.54	3.57
FSC threshold	0.143	0.143	0.143
Map sharpening B factor ($Å^2$)	-50	-50	-50
Refinement			
Model resolution (Å)	3.88	3.54	3.57
Model composition			
Non-hydrogen atoms	33576	33576	33576
Protein residues	4300	4300	4300
Ligands	4 NAD^+	4 NAD^+	4 NAD^+
B factors ($Å^2$)			
Protein	224.33	189.71	159.33
Ligands	273.06	208.84	186.14
R.m.s. deviations			
Bond lengths (Å)	0.001	0.002	0.002
Bond angles (°)	0.371	0.409	0.395
Validation			
MolProbity score	1.69	1.62	1.50
Clashscore	10.54	11.11	9.42
Poor rotamers (%)	0.11	0	0.11
Ramachandran plot			
Favored (%)	97.20	97.76	98.55
Allowed (%)	2.80	2.24	1.45
Disallowed (%)	0	0	0
CC (mask)	0.83	0.77	0.83
CC (box)	0.91	0.87	0.89
CC (peaks)	0.77	0.70	0.77
CC (volume)	0.82	0.76	0.82
Mean CC for ligands	0.85	0.82	0.80

662

	empty-monomer (EMD-52422)	cofactor-monomer (EMD-52423)	cofactor/ligand-monomer (EMD-52424)
Data collection and			
Magnification	130,000	130,000	130,000
Voltage (kV)	300	300	300
Electron dose ($e^-/Å^2$)	0.979	0.979	0.979
Defocus range (μm)	1.0-1.6	1.0-1.6	1.0-1.6
Pixel size (Å)	1.29	1.29	1.29
Symmetry imposed	C1	C1	C1
Initial particles images (no.)	464,320	464,320	464,320
Final particles images (no.)	131,216	168,668	112,701
Map resolution (Å)	3.07	2.95	3.12
FSC threshold	0.143	0.143	0.143
Map sharpening B factor	LS	LS	LS
Refinement			
Model resolution (Å)	3.07	2.95	3.12
Model composition			
Non-hydrogen atoms	8717	8761	8760
Protein residues	1124	1124	1123
Ligands	-	1 NAD^+	1 NAD^+/ 1 L-Glu
B factors ($Å^2$)			
Protein	64.32	62.58	72.09
Ligands	-	56.65	81.37
R.m.s. deviations			
Bond lengths (Å)	0.004	0.004	0.004
Bond angles (°)	0.691	0.721	0.693
Validation			
MolProbity score	1.37	1.27	1.37
Clashscore	5.53	5.16	5.80
Poor rotamers (%)	0.55	0.55	0.11
Ramachandran plot			
Favored (%)	97.68	98.48	97.77
Allowed (%)	2.32	1.52	2.23
Disallowed (%)	0	0	0
CC (mask)	0.87	0.88	0.87
CC (box)	0.89	0.89	0.89
CC (peaks)	0.81	0.81	0.79
CC (volume)	0.88	0.88	0.87
Mean CC for ligands	-	0.91	0.84

663

	Open-cofactor/ligand-monomer (EMD-52425)	**Closed1-cofactor/ligand-monomer** (EMD-52426)	**Closed2-cofactor/ligand-monomer** (EMD-52427)
Data collection and			
Magnification	130,000	130,000	130,000
Voltage (kV)	300	300	300
Electron dose (e^-/Å^2)	0.979	0.979	0.979
Defocus range (μm)	1.0-1.6	1.0-1.6	1.0-1.6
Pixel size (Å)	0.646	0.646	0.646
Symmetry imposed	C1	C1	C1
Initial particles images (no.)	112,701	112,701	112,701
Final particles images (no.)	33,330	46,380	32,991
Map resolution (Å)	3.23	3.11	3.18
FSC threshold	0.143	0.143	0.143
Map sharpening B factor	LS	LS	LS
Refinement			
Model resolution (Å)			
Model composition			
Non-hydrogen atoms			
Protein residues			
Ligands			
B factors (Å^2)			
Protein			
Ligands			
R.m.s. deviations			
Bond lengths (Å)			
Bond angles (°)			
Validation			
MolProbity score			
Clashscore			
Poor rotamers (%)			
Ramachandran plot			
Favored (%)			
Allowed (%)			
Disallowed (%)			
CC (mask)			
CC (box)			
CC (peaks)			
CC (volume)			
Mean CC for ligands			

664

	total-monomer (EMD-52428)	**Closed2-cofactor/ligand-tetramer** (EMD-52429)
Data collection and		
Magnification	130,000	130,000
Voltage (kV)	300	300
Electron dose ($e^-/Å^2$)	0.979	0.979
Defocus range (μm)	1.0-1.6	1.0-1.6
Pixel size (Å)	0.646	1.29
Symmetry imposed	C1	C1
Initial particles images (no.)	464,320	112,701
Final particles images (no.)	464,320	32,991
Map resolution (Å)	2.63	4.10
FSC threshold	0.143	0.143
Map sharpening B factor	LS	-50
Refinement		
Model resolution (Å)	2.63	
Model composition		
Non-hydrogen atoms	8683	
Protein residues	1113	
Ligands	1 NAD^+	
B factors ($Å^2$)		
Protein	56.19	
Ligands	48.51	
R.m.s. deviations		
Bond lengths (Å)	0.002	
Bond angles (°)	0.467	
Validation		
MolProbity score	1.39	
Clashscore	7.12	
Poor rotamers (%)	0.55	
Ramachandran plot		
Favored (%)	99.10	
Allowed (%)	0.90	
Disallowed (%)	0	
CC (mask)	0.80	
CC (box)	0.68	
CC (peaks)	0.65	
CC (volume)	0.78	
Mean CC for ligands	0.81	

665

666 **FIGURES**

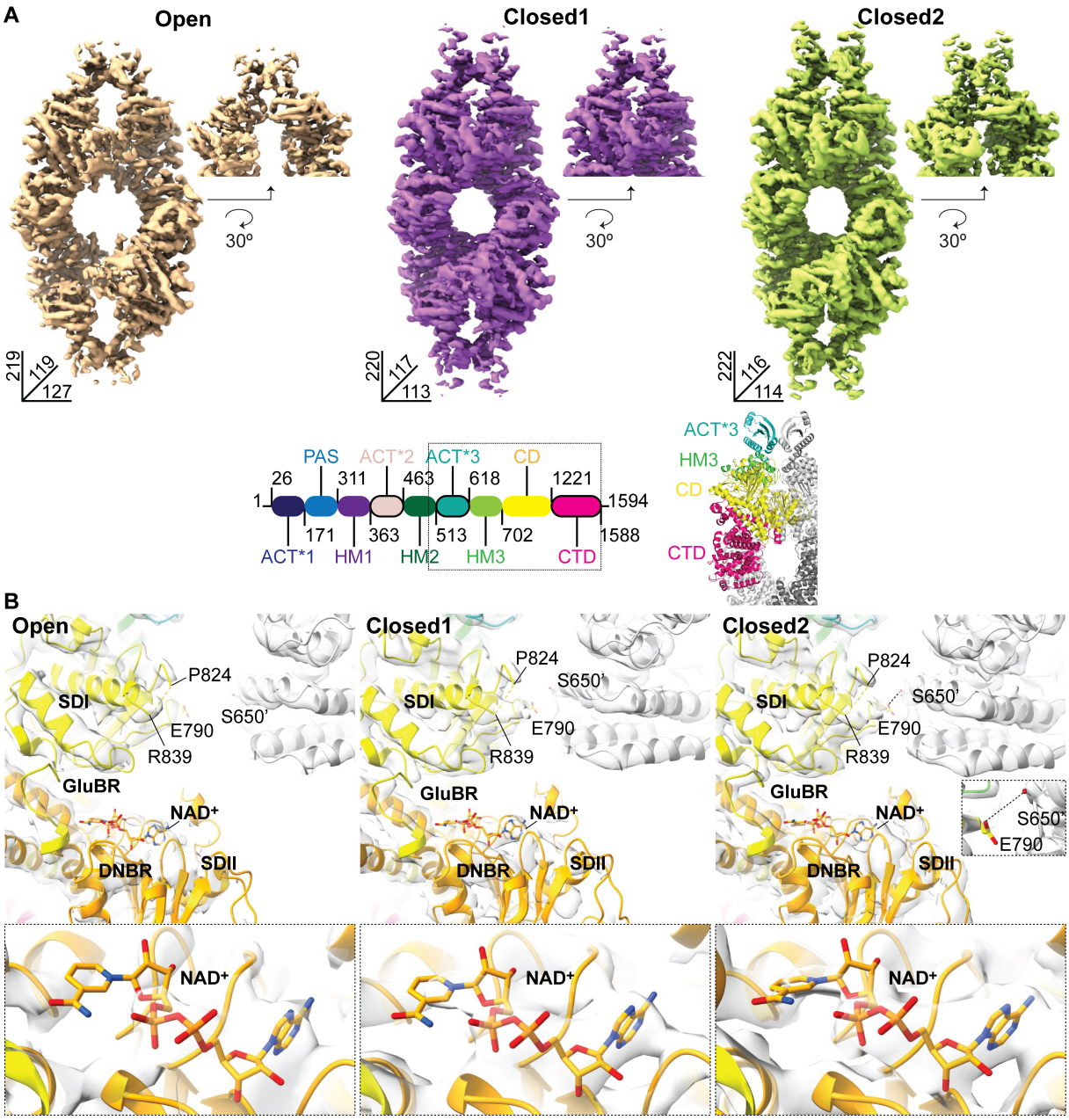

667

668 **Figure 1**

669 **Three conformers of mL-GDH$_{180}$ detected upon incubation with L-glutamate**

670 **and NAD$^+$ reveal modulations of the enzyme quaternary structure.** (A) Cryo-EM

671 mL-GDH$_{180}$ maps obtained after incubating the enzyme with L-glutamate and NAD$^+$.

672 The dimensions of each conformer are provided in Å. Maps cover, for each

673 monomer, the region indicated by a dotted rectangle in the diagram shown below

674 (residues 500-1588). ACT*, Aspartate kinase-Chorismate mutase-TyrA-like; PAS,

675 Per-Arnt-Sim; HM, helical motif; CD, catalytic domain; CTD, C-terminal domain. (B)
676 Approach of the catalytic domains of mL-GDH_{180} subunits linked by the N-terminal
677 region. Segment 825-838, poorly defined in maps of the Open, Closed1 and Closed2
678 enzyme forms, approaches the catalytic domain in a neighboring subunit. In each
679 case, a zoomed in view of the dinucleotide binding region (DNBR) is shown below.
680 The protein is displayed in ribbon representation and cryo-EM maps are depicted in
681 grey. The nicotinamide portion of the NAD^+ molecule (in sticks) exhibits high mobility
682 in all conformations. Subdomains I and II (SDI and SDII) of the catalytic domain are
683 colored in yellow and orange, respectively, whereas ACT*3 and HM3 motifs are
684 shown in cyan and green, respectively, for one monomer (the one on the left), with
685 the neighboring subunit (the one on the right) shown in grey. All maps are shown with
686 a contour level of 0.02. GluBR, glutamate binding region.
687

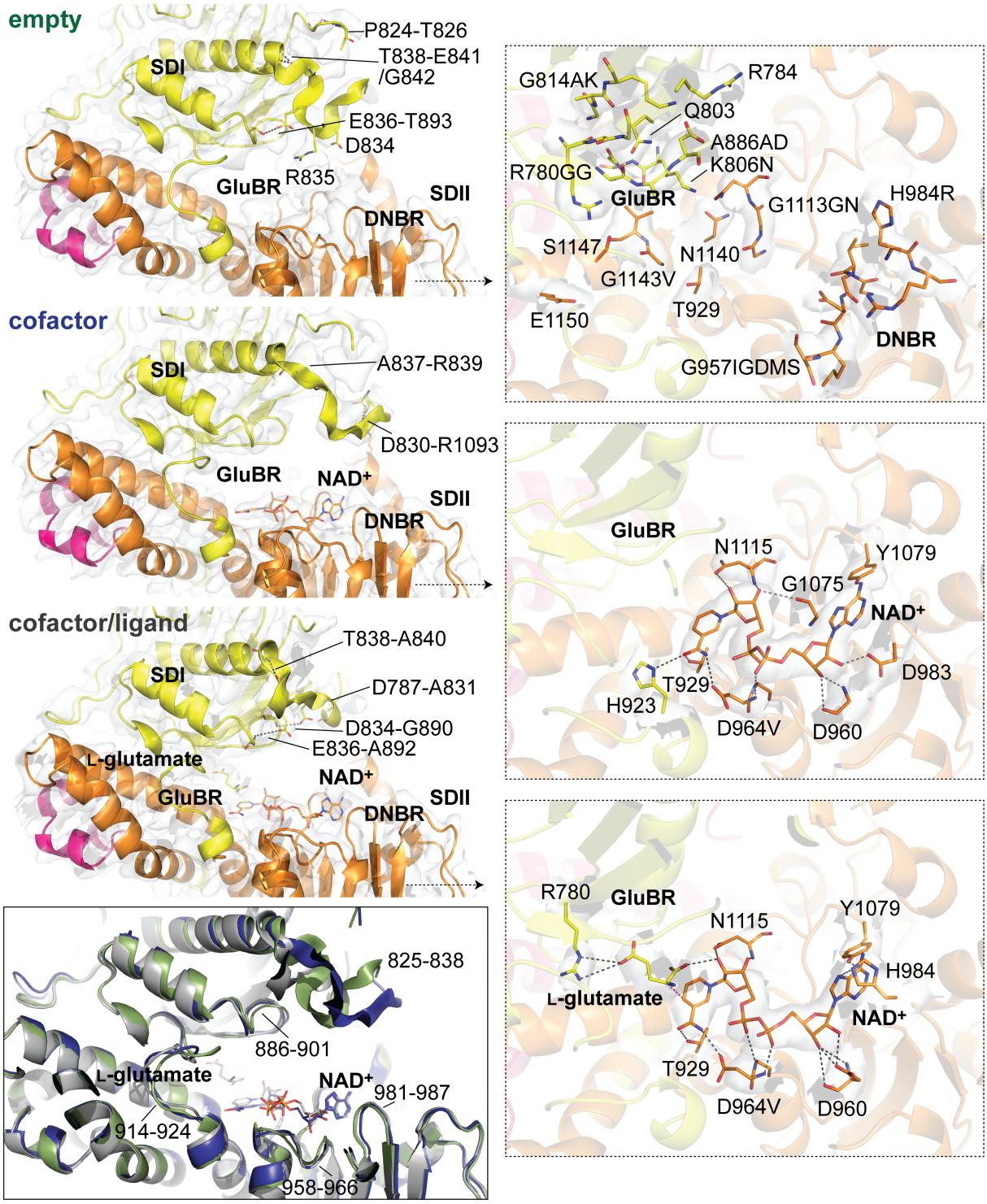

Figure 2

Three conformers of mL-GDH$_{180}$ subunits reveal modulations in tertiary structure associated with differential active site occupancies. Alternative conformations of mL-GDH$_{180}$ subunits are shown, with the active site either empty or containing NAD$^+$ or NAD$^+$ and L-glutamate. The average RMSD for 1122 aligned

residues in pairwise comparisons of the atomic models (show in ribbon representation) is 0.7 Å. NAD^+ and L-glutamate are depicted as sticks as well as highlighted residues. For each species, subdomains I and II of the catalytic domain (SDI, residues 702-926 and 1188-1220; SDII, residues 927-1187) are colored in yellow and orange, respectively. A small portion of the C-terminal domain is displayed in magenta. Interactions established by the segment 825-838 with other portions of the polypeptide chain are shown in the panels on the left. Note that within the region 825–838, residues 825-827 and 830-838 could be built for the empty- and cofactor- monomers, while residues 825 and 829-838 were modeled for the cofactor/ligand-monomer. A comparison of the atomic models of the empty- (green), cofactor- (blue) and cofactor/ligand-monomer (gray) is presented in the lower left corner. Cryo-EM maps are depicted in grey, with contour levels of 5. H-bonds and salt bridges are displayed as dashed lines. GluBR, glutamate binding region; DNBR, dinucleotide binding region.

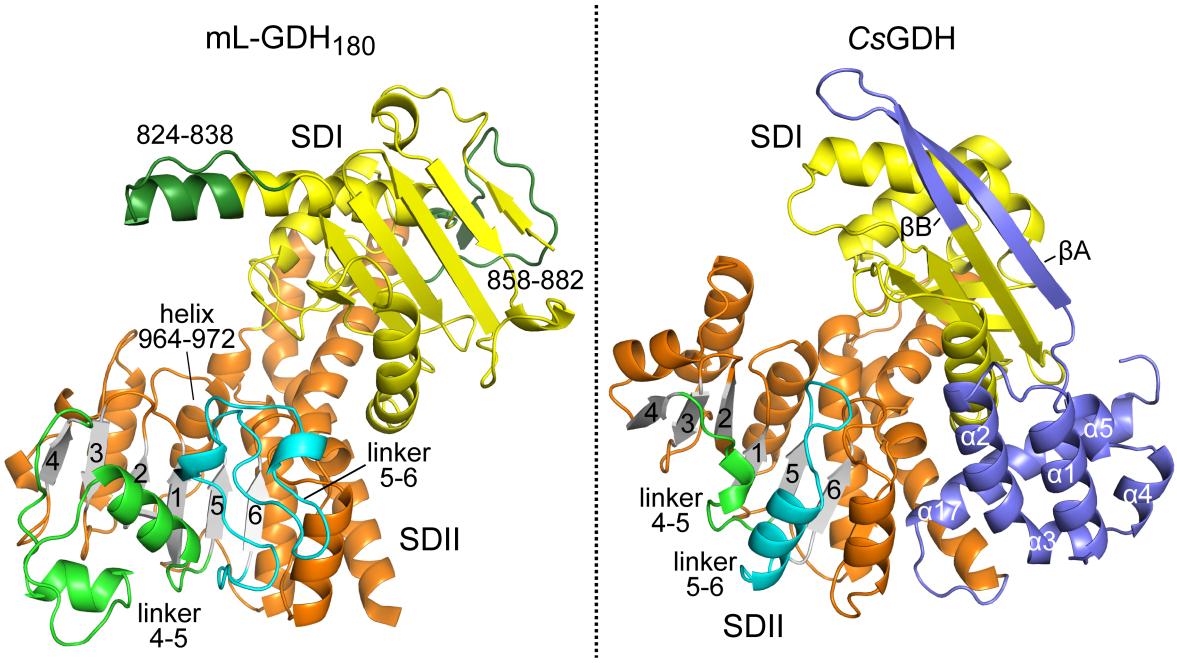

Figure 3

Comparison of the catalytic domain of mL-GDH$_{180}$ with that of S-GDHs. A monomer of mL-GDH$_{180}$ is shown on the left. Segments 824-838 and 858-882 (in dark green), both located in the catalytic domain subdomain I (SDI), are absent in S-GDHs [2]. For the 824-838 portion coordinates were taken from a model calculated with AlphaFold 3 [33]. A monomer of *Cs*GDH (*Cs*, *Clostridium symbiosum*; PDB 1BGV [20]), considered a representative S-GDH, is shown on the right. The SDI of S-GDHs presents secondary structure elements (in dark blue, named according to the consensus nomenclature for S-GDHs) with conserved roles in oligomerization in the enzyme subfamily, which are not present in mL-GDH$_{180}$ or related L-GDHs. For both mL-GDH$_{180}$ and *Cs*GDH, the six-stranded 432156 β-sheet that shapes the DNBR in the catalytic domain subdomain II (SDII) is shown in grey; the linker regions β4-β5 (in light green) and β5-β6 (in cyan) encompass a larger number of residues in mL-GDH$_{180}$. For the two proteins, the SDI and SDII are shown, except for otherwise highlighted portions, in yellow and orange, respectively.

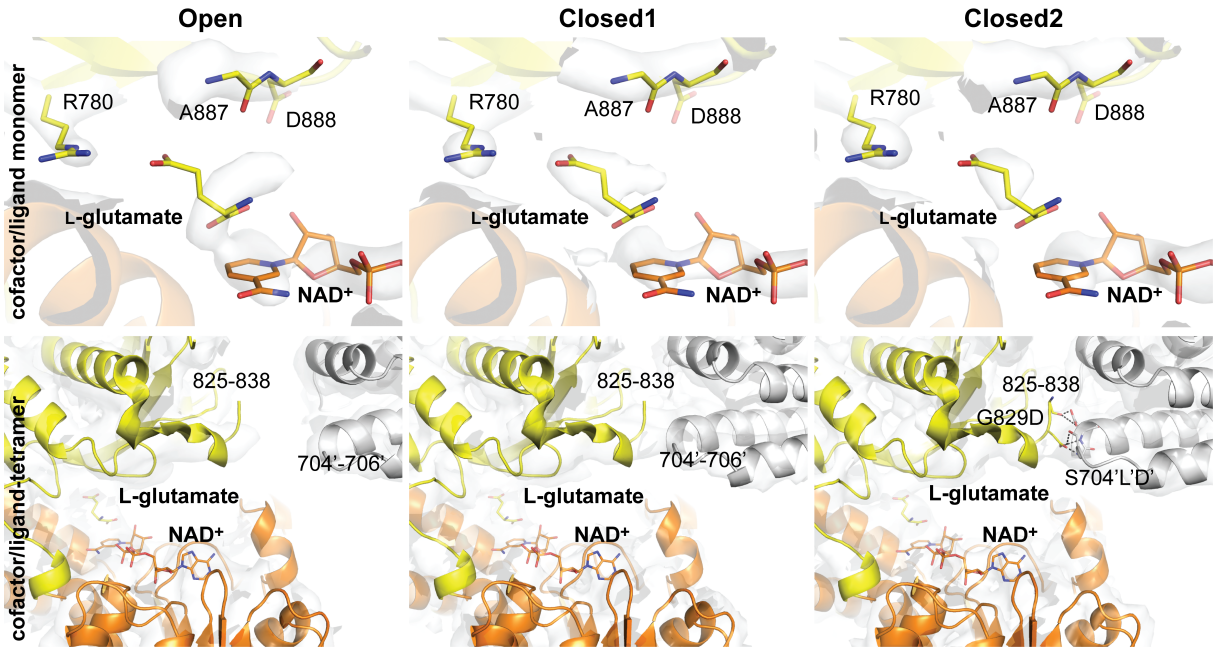

726

727 **Figure 4**

728 **GluBR occupancy is linked to the coupling of the catalytic domain of two**
729 **adjacent monomers in the Closed conformations.** Top panel: the atomic model of
730 the cofactor/ligand-monomer of mL-GDH$_{180}$ is shown together with maps of this
731 species obtained from Open, Closed1 or Closed2 tetramers (Open-, Closed1- and
732 Closed2- cofactor/ligand-monomers; contour levels are 5). NAD$^+$ and L-glutamate as
733 well as highlighted residues are depicted as sticks. The subdomains I and II of the
734 catalytic domain (SDI and SDII) are colored in yellow and orange, respectively.
735 Bottom panel: in the context of tetramers containing a cofactor/ligand-monomer
736 (cofactor/ligand-tetramers; contour levels are 0.015), in a progression towards the
737 Closed1 and Closed2 conformers, the stabilization of an interaction between
738 segment 825-838 of one subunit (colored, on the left) and segment 704-706 of the
739 neighboring one (in grey, on the right) is observed. The atomic coordinates of the
740 subunit on the left correspond in each case to those of a cofactor/ligand-monomer,
741 replacing the equivalent ones presented in Figure 1. H-bonds and salt bridges are
742 displayed as dashed lines. Cryo-EM maps are displayed in grey.

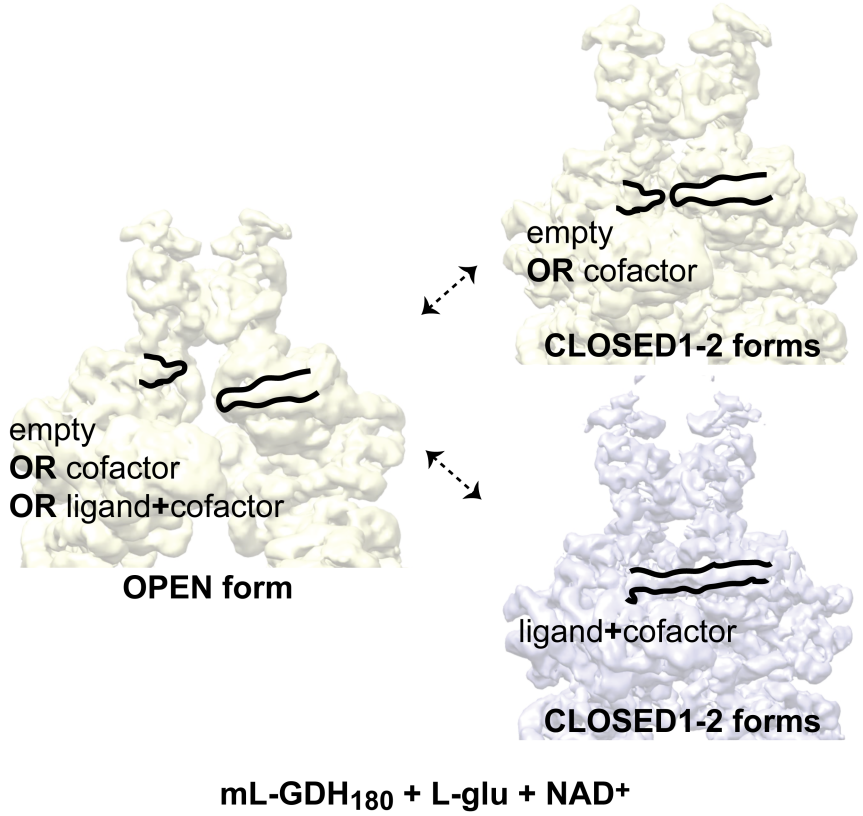

Figure 5

Ligand binding triggers tertiary structure remodeling that links catalysis with intersubunit communication in mL-GDH$_{180}$. Cryo-EM maps of mL-GDH$_{180}$ incubated with L-glutamate and NAD$^+$ illustrate the conformational ensemble comprising one open and two closed tetrameric states. In the open form, active sites can be empty or occupied by the cofactor or by both cofactor and ligand. In the closed conformations, when both the cofactor and the substrate simultaneously occupy the active site, the catalytic domains of neighboring subunits connected through their N-terminal regions approach each other, forming an intersubunit contact approximately 2 nm away from the catalytic center bearing the ligand and cofactor. This structural transition provides a physical link between active-site occupancy and long-range communication within the tetramer, coupling catalysis to quaternary-structure remodeling.